


Active Control of Terahertz Waves Using Vanadium-Dioxide-Embedded Metamaterials

Caihong Zhang,¹ Gaochao Zhou,¹ Jingbo Wu,¹ Yahua Tang,² Qiye Wen,² Shaoxian Li,³
 Jiaguang Han,³ Biaobing Jin,^{1,*} Jian Chen,¹ and Peiheng Wu¹

¹*Research Institute of Superconductor Electronics (RISE), School of Electronic Science and Engineering,
 Nanjing University, Nanjing 210023, China*

²*State Key Laboratory of Electronic Thin Films and Integrated Devices, University of Electronic Science and
 Technology of China, Chengdu 610054, China*

³*Center for Terahertz Waves, College of Precision Instrument and Optoelectronics Engineering,
 and the Key Laboratory of Optoelectronics Information and Technology (Ministry of Education),
 Tianjin University, Tianjin 300072, China*

 (Received 4 January 2019; revised manuscript received 18 February 2019; published 7 May 2019)

We describe a method for the active control of terahertz (THz) waves using vanadium dioxide (VO₂)-embedded hybrid metamaterials (MMs). VO₂ undergoes an insulator–metal phase transition at around 68 °C, causing its conductivity to change by five orders of magnitude. Our MM consists of a periodic array of two metallic structures connected with VO₂ pads. Simulations show that this MM can realize mode switching via the VO₂ pads with high conductivity in the conduction state and high dynamic conductivity across the phase transition. Such material characterizations have rarely been observed in other materials, such as semiconductors, superconductors, and graphene. More interestingly, this mode switch can be realized experimentally using not only a thermal stimulus, but also electrical and optical stimuli. The phase transition mechanisms are the same for thermal and electrical stimuli, but different for the optical stimulus. This diverse range of stimuli is very useful for manipulating the THz waves in practical applications.

DOI: [10.1103/PhysRevApplied.11.054016](https://doi.org/10.1103/PhysRevApplied.11.054016)

I. INTRODUCTION

The fifth-generation (5G) wireless network is currently deployed across the world. This means it is important to accelerate fundamental research on the next-generation, i.e., sixth-generation (6G), network [1]. It has been reported that, to satisfy the demand for system bandwidth, capacity, and transmission rate, the working frequency for the 6G network may be elevated to 140, 220, and 340 GHz, which are located in the sub-terahertz (THz) regime. Moreover, the sub-THz spectrum is currently sparsely occupied, making it suitable for future wireless communications [2]. Thus, there is considerable interest in the development of novel sub-THz sources, functional devices, and detectors [3].

At present, sub-THz devices are still relatively immature; for example, the source power is too low to transmit signals over long distances in free space [3], the detector cannot achieve very high sensitivity at room temperature [4], and there is a lack of tunable materials

for sub-THz functional devices [4]. The physical reason is that conventional electronic and optical methods of device design used in the adjacent microwave and infrared light bands cannot easily be extended to the sub-THz regime. Therefore, alternative materials and design principles for developing high-performance sub-THz devices are urgently needed.

MMs have a periodic structure that enables the construction of artificial materials with arbitrary equivalent permittivity and permeability through the elaborate design of unit cell structures [5,6]. In recent decades, MMs have offered an innovative paradigm for the design of alternative electromagnetic functional devices. To make these functional devices more powerful, the active MMs can incorporate active components and tunable materials. At the THz level, the main tunable materials are semiconductors [7–10], liquid crystals [11,12], phase-change materials such as VO₂ [13–20], superconductors [21–26], and 2D materials such as graphene [27–29]. Their conducting or dielectric properties can be tuned or switched by thermal, optical, magnetic, and electrical stimuli. For active MMs, the functions of frequency-tuning or switching resonant modes can be realized through an elaborate MM design. For example, we can incorporate photoconductive semiconductors into

*bbjin@nju.edu.cn

MM-based devices to manipulate their THz response via an optical stimulus [9,10].

Among these tunable materials, VO₂ is very prominent in the THz community because of its large and steep change of conductivity across a metal-insulator transition [30–32]. When the working temperature is above 68 °C, just a little higher than room temperature, the lattice of VO₂ begins to change from an insulating monoclinic phase to a metallic tetragonal phase. The conductivity changes by approximately 4–5 orders of magnitude during this transition. Moreover, optical and electrical stimuli can also bring about this phase transition [32,33]. In particular, VO₂ has a subpicosecond response time to an optical stimulus [34]. These diverse stimuli, low working temperature, and good performance make VO₂ a popular choice for potential applications.

In this paper, we design a VO₂-embedded hybrid MM to realize mode switching [35–38]. This mode switch, analogous to the resonant mode switching phenomenon in plasmonics, requires a functional material with a large dynamic conductivity range and high conductivity in the conducting state. We once attempted to use superconducting (SC) materials, which changed their electrical conductivity across the SC transition [35], but this resonant mode switch did not occur because of the relatively small change of conductivity during the transition. In our present work, this mode switch is successfully observed in a VO₂-embedded hybrid MM, which shows its unique tuning capability compared with superconductors. Additionally, the switches are observed experimentally in the cases of optical and electric stimuli. Moreover, we find that the change in resonant frequencies for thermal and electric stimuli is different to that produced by an optical stimulus. The relations between the thermal, electrical, and optical stimuli and the underlying physical process are also discussed.

II. DESIGN AND SIMULATIONS

There are several THz MM-based devices that use VO₂ films or pads as thermal- or electrical-sensitive elements [13–18]. For example, a switchable ultrathin quarter-wave plate with VO₂ pads inserted in the resonator of the MM element has been reported [14]. To demonstrate the unique tuning performance of VO₂ film, which is barely matched by common THz tuning materials, four types of hybrid resonators are designed and simulated and the resonance mode switch in VO₂-hybrid MMs is investigated [17]. This mode transition is very useful for making THz modulators. The tunable THz transmission is also observed in an electrically controlled THz resonator with VO₂ film [18].

In this section, we describe the simulation of the THz spectra using electromagnetic field computational software. Figure 1 shows the VO₂-embedded hybrid MM studied in this paper. Resonant mode switching occurs

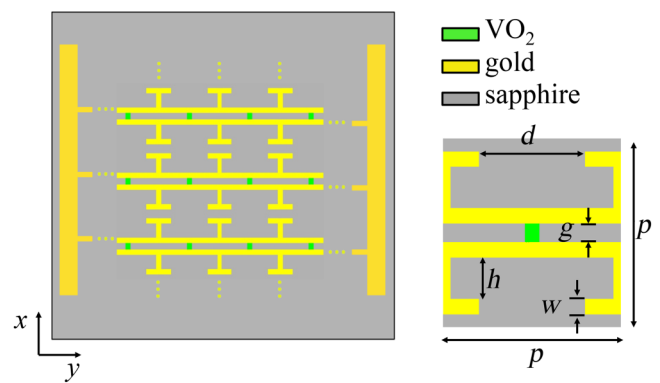


FIG. 1. Left: Schematic diagram of MM embedded with 200-nm thick VO₂ film (green color). Right: Geometric parameters of unit cell of the MM, $p = 100 \mu\text{m}$, $g = 10 \mu\text{m}$, $w = 8 \mu\text{m}$, $d = 60 \mu\text{m}$, $h = 22 \mu\text{m}$.

when the VO₂ film transits from low conductance to high conductance states. The unit cell of the MM is shown on the right of Fig. 1. It consists of two folded gold wire structures connected with a VO₂ pad, which we refer to as a dimer. The geometrical parameters of the unit cell are $p = 100 \mu\text{m}$, $g = 10 \mu\text{m}$, $w = 8 \mu\text{m}$, $d = 60 \mu\text{m}$, and $h = 22 \mu\text{m}$. The gold and VO₂ layers are both 200-nm thick. When the VO₂ film changes from insulator to metal, the THz response along the x direction experiences remarkable changes as a result of the resonant mode switching. The film mimics dimer pairs made from two subwavelength plasmonic particles, which suggests promising applications in sensing, local field enhancement, and high-frequency conductance probing [35–37].

The resonant mode switching properties of the MM can be illustrated using a three-dimensional full wave simulation in the commercial software CST Microwave Studio. To illustrate the role of the conductive coupling, the VO₂ pad in the simulation is first replaced by a normal material with a real part of relative dielectric constant of 1 and a set of electrical conductivities. In the case of x direction polarization and normal incidence, the THz transmission spectra of the structure at conductivities of 40 S/m and 4×10^5 S/m in the VO₂ film region are shown in Fig. 2. As shown in Fig. 2(a), there is a switch from a resonant dip (labeled A) to two resonant dips (labeled B and C). Figures 2(b)–2(d) show the simulated electric field distributions corresponding to points A , B , and C , respectively. According to the simulated electric field distribution and the maximum position of the charge density in Fig. 2(b), the resonant mode at point A can be considered as a hybrid of the two electric dipole resonances. In particular, a simulation analysis of the resonant mode indicates that it is similar to a bonding dimer plasmonic (BDP) mode [36]. For the BDP mode, the center of the gap between the upper and lower metal structures is located at the position of the VO₂ pads, the ends of which have the largest charge

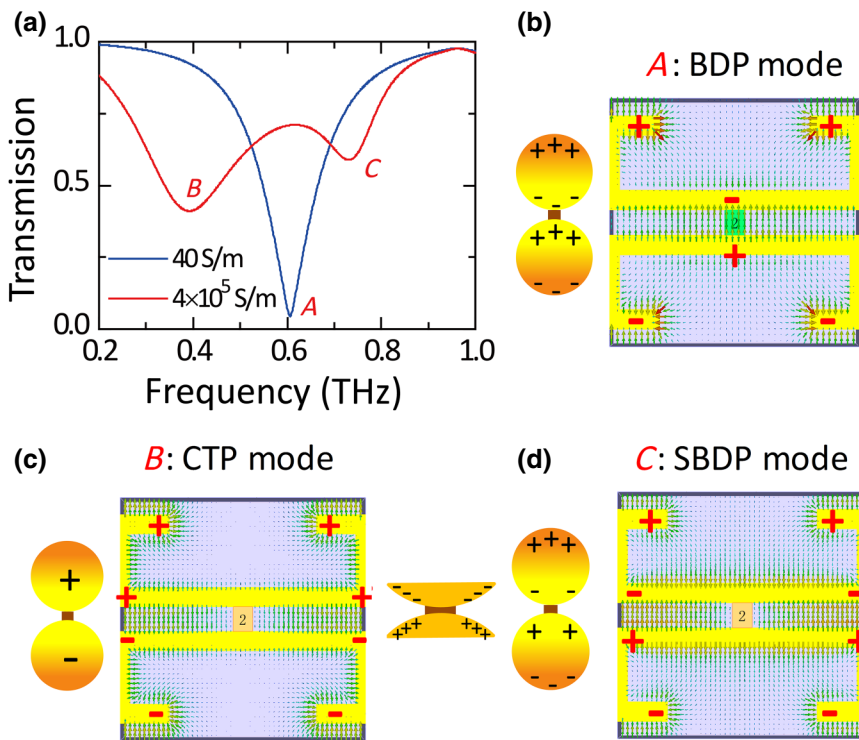


FIG. 2. Simulation analysis of resonance modes. (a) Transmission spectrum of the MM with VO₂ pad conductivities of 40 S/m and 4×10^5 S/m, respectively. (b-d) Distributions of the electric fields and charges for BDP, CTP, and SBDP modes. The red + and - denote positive and negative charge distribution densities, respectively.

density. When the VO₂ film becomes a good conductor, conductance coupling occurs between the upper and lower parts of the metallic structure. This allows the charge to flow through the gap to produce two resonance modes. The distributions of the electric fields and the charges for two modes are depicted in Figs. 2(c) and 2(d). For the resonance at point B, only one kind of charge is distributed in each part of the metal structure [Fig. 2(c)], and the total net charge appears in each part. These features are similar to the charge transfer plasmonic (CTP) mode [36]. At point C, there is another pattern [Fig. 2(d)], which has opposite charges on each part, much like the BDP pattern in Fig. 2(b). The difference is that the local electric field in the center of the gap is shielded as the VO₂ region becomes highly conductive, so this mode is also called the screened BDP (SBDP) mode [36].

In the case of *x* direction polarization and normal incidence, the THz transmission spectra of the structure for various conductivities in the VO₂ region are presented in Fig. 3. When VO₂ is in the insulator state, the BDP mode dominates and there is only one resonance dip in the transmission spectrum. As the conductivity increases in the VO₂ region, the spectral response exhibits continuous changes. Both the amplitude at the resonance frequency and the resonance frequency itself increase with the conductivity. As the conductivity increases from 1.6×10^5 S/m to 2×10^5 S/m, the resonant mode splits into two, as shown in the transmission spectra. One resonance mode shows a slight blueshift relative to the initial BDP resonance. In the previous description, the high-frequency

resonance is the SBDP mode generated by conductance coupling, whereas the low-frequency resonance is the CTP mode. With a further increase in conductivity, the quality factors of these two resonances gradually increase. It can be seen that the aforementioned resonant mode-switching process occurs when the conductivity increases from 4×10^4 S/m to 5×10^5 S/m. To achieve resonance switching, therefore, the conductivity variation should cross the critical value of 2×10^5 S/m.

Several material candidates can realize conductivity variations under environmental or stimulus changes. For example, the semiconductor silicon-on-sapphire changes

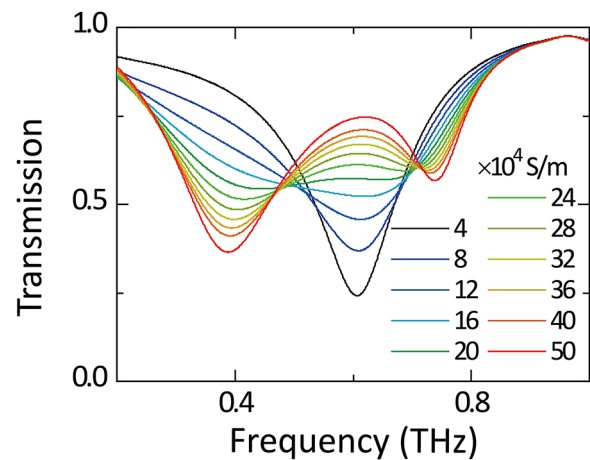


FIG. 3. Simulated transmission as a function of the conductivity of VO₂ thin film.

from approximately 1 to approximately 10^4 S/m [8]. The conductivity of Yttrium Barium Copper Oxide (YBCO) SC materials is approximately 10^5 S/m in normal state and approximately 10^6 S/m in the SC state, a change of one order of magnitude [21,22]. The surface conductivity of chemical vapor deposition-grown graphene can be adjusted from approximately 0.1 mS to several mS by changing the voltage [28,29,39]. Our previous experimental study on SC NbN film supports this conclusion [35]. VO₂ exhibits a change in conductivity of approximately 5 orders of magnitude, providing a larger dynamic range as it undergoes the phase transition [40]. This enables some unique properties in terms of manipulating THz waves. In the following section, we present an experimental demonstration of mode switching under thermal, electrical, and optical stimuli, and describe a powerful material for manipulating THz waves.

III. EXPERIMENTAL RESULTS

A. Sample preparation

A thin VO₂ film is deposited on a 500- μ m thick *c* cut sapphire substrate by reactive magnetron sputtering [41]. The sputtering target is vanadium metal with a purity of 99.99%. The vacuum chamber is first evacuated to 10^{-4} Pa, and then the sapphire substrate is heated and kept at 550 °C. A mixture of high-purity Ar and oxygen (O₂/Ar ratio = 5%) is poured into the chamber to stabilize the base pressure at approximately 1.0 Pa. The rf source gun power is set to 200 W. Before the deposition, the surface of the vanadium target is cleaned by presputtering for at least 10 min. A film with a thickness of approximately 200 nm is then deposited onto the substrate. Finally, the sample temperatures are lowered to 450 °C for 30 min and then 200 °C for 30 min before being naturally cooled to the ambient temperature in air.

The samples are prepared using photolithography and a micro-fabrication process. First, the VO₂ layer is patterned via reactive ion etching with CF₄ of 40 sccm (standard-state cubic centimeter per minute) fluence and 100 W rf power after photolithography. Gold films are then deposited on the samples by electron beam evaporation following the second photolithography. Eventually, the samples are fabricated using the lift-off process.

B. Thermal stimulus case

First, we investigate the THz response of the VO₂-embedded MM under a thermal stimulus using traditional THz time domain spectroscopy (THz TDS). See Supplemental Material for the measurement detail [42]. Transmission spectra are measured at different temperatures spanning the metal–insulator phase temperature of approximately 68 °C. The transmission spectrum obtained using a Fourier transform is shown in Fig. 4(a). It can be seen

from Fig. 4(a) that resonance occurs at 0.62 THz when the temperature is 51 °C, which corresponds to the BDP mode. When the temperature increases to 70 °C, the resonant frequency exhibits a redshift and the THz transmission amplitude at the resonance frequency increases. Note that the redshift of the resonance frequency is different from the simulation results. This is because both the electrical conductivity and the real part of the dielectric constant increase during the phase transition of VO₂ film [40,43], which leads to an increase in capacitance between the upper and lower metallic structures. Therefore, the resonance frequency for the BDP mode shifts to a lower value. When the temperature rises to 71 °C, the phase transition occurs, and there is no longer a single Lorentz resonance in the transmission spectra. As the temperature increases by 0.5 °C, the two resonant modes appear in the spectrum, which indicates that the MM has changed from BDP mode to SBDP and CTP modes. When the temperature rises in the range of 72–88 °C, the increase in conductivity of the VO₂ leads to a decrease in the Ohmic loss of the CTP and SBDP modes and an increase in the strength of the resonance. The amplitude modulation depths of the THz wave in this VO₂-embedded hybrid MM are 82% and 89% at 0.41 and 0.62 THz, respectively, in the thermal stimulus case.

C. Electrical stimulus case

Compared with the thermal stimulus case, an electrical stimulus has the advantages of convenience and reliability. Figure 4(b) presents the THz transmission spectra of the device for various bias currents at room temperature. It can be seen that the BDP resonance mode occurs at 0.62 THz and is almost unchanged when the current is below 0.2 A. When the current increases from 0.26 A to 0.31 A, the BDP mode frequency of our VO₂-embedded hybrid MM shifts toward the red end of the spectrum and the resonance bandwidth increases, which is consistent with the phenomenon in the thermal stimulus case. This indicates that the dielectric constant and conductivity of the VO₂ thin film both increase when an electrical stimulus is applied. When the current increases from 0.31 A to 0.32 A, the resonance of the MM immediately changes from the BDP mode to the CTP and SBDP modes. When the current increases to 0.35 A, the THz transmission became saturated, which is very similar to the thermal stimulus case. To observe the variation in the transmission spectra with the applied electrical current, Fig. 4(c) shows the transmission amplitude changes with respect to the electrical current at 0.41 and 0.62 THz. It can be seen that the 0.62 THz case exhibits better linearity than that at 0.41 THz. The transmission amplitude at 0.62 THz varies nearly linearly with the applied current in the range 0.28–0.33 A, which is suitable for amplitude modulation. In this range, the transmission varies from 0.38 to 0.76, and the modulation depth is 75%.

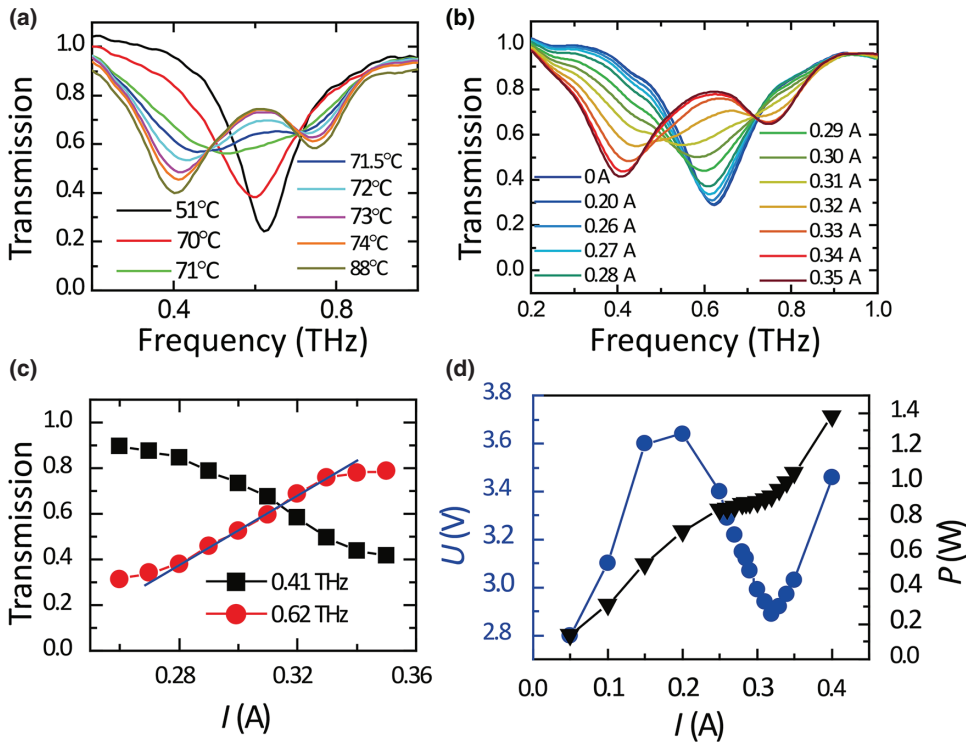


FIG. 4. (a) THz spectra at different temperatures spanning the transition temperature of the VO₂ thin film. (b) THz spectra at different bias currents at room temperature. The resonance dip splits into two resonance dips at 0.31 A, which indicates the start of phase transition in the VO₂ thin film. (c) Transmission as a function of bias current at 0.41 THz (black square) and 0.62 THz (red dot). (d) I - V characteristics of the MM (black) and the absorption power of the MM (blue) at different currents.

There are two possible mechanisms for the VO₂ phase transition. One is the electric-induced phase transition [44–48], the other is the Joule-heat-induced phase transition. The first comes from the electric field Poole-Frenkel effect, or carrier injection, which leads to an increase in the carrier concentration. When the concentration reaches the critical value (approximately 10^{21} cm⁻³) required for phase transition [49], the VO₂ film undergoes the Mott phase transition, that is, the metastable metal phase breaks down under the strong electric field [50]. The lattice structure of the VO₂ material (monoclinic lattice metal) remains unchanged during the transition, and only electronic phase transition takes place. The electronic phase transition then causes the lattice structure to change. Finally, the film completes the Peierls structural phase transition. The second mechanism, Joule-heat-induced phase transition, is caused by the current in VO₂ films. This produces Joule heat, causing the temperature to exceed the critical temperature required for phase transition. The trigger for phase transition depends on the carrier injection or the Poole-Frenkel field effect to provide the electrical current, and the Joule heat produced by the electrical current is sufficient for thermal-induced phase transition before the carrier concentration reaches the critical value for the Mott phase transition [51–54]. According to a previous study [55], the field strength of the critical electric field of the electro-induced phase transition is approximately 50 V/ μ m. In our experiment, the maximum electric field is much lower at approximately 2.1 V/ μ m. Therefore, the thermally induced Joule phase transition should occur in our VO₂ thin film

in the electrical stimulus case. Figure 4(d) shows the I - V (current–voltage) characteristic and the absorption power P ($P = U \times I$) of our VO₂-embedded hybrid MM. It can be seen that in the current range 0.2–0.32 A, the I - V curve of the device exhibits negative differential resistance, which is caused by the VO₂ phase transition. The absorption power indicates that the power consumption of the device is less than 1 W, and this could be reduced further by reducing the area of the device.

Because the VO₂ phase transition in our electrical stimulus case is caused by Joule heat, the speed of the electrical stimulus is limited by the thermal response time of the film. In addition, the electrical parameters of the MM affect the response time. In our MM, there is a large capacitance between the parallel metal lines in the structure, which will prolong the response time.

D. Optical stimulus case

We conduct an optical stimulus experiment using the optical pump–THz probe spectroscopy. See Supplement Material for the detail of experimental setup [42,56,57], which provides an alternative method of controlling THz wave transmission. Interestingly, different from the electrical stimulus case, the response time is not related to the geometrical electric parameters. As we know, the effect induced by the thermal and electrical stimulus is mainly the thermal effect, therefore, the switching time can not be as fast as optical stimulus, as it depends on the temperature, electrical current, the sample geometrical parameters, the

external substrate, and so on. The switching time for these two cases is estimated to be on the orders of subseconds. In our optical stimulus case, the central wavelength of the pump pulse is 800 nm, corresponding to a photon energy of 1.55 eV, which is larger than the insulation phase gap of 0.67 eV [14]. The maximum power of the pulse after the L4 lens measured to be 2.2 W, and the energy density calculated to be approximately 6.6 mJ/cm² based on the spot size. There is a threshold of light energy density for the phase transition of the VO₂ film, which is reported to be 7 mJ/cm² for a 100-nm thick film on MgO substrate [58]. Therefore, the maximum optical energy density of the femtosecond pulse may be lower than the threshold. The THz transmission of the VO₂-embedded hybrid MM is almost unchanged at room temperature under the maximum optical pump power. To measure the change in THz transmission through the MM under an optical stimulus, we heat the sample to slightly below the phase transition temperature to reduce the threshold of the optical excitation energy density.

Figure 5 shows the THz transmission spectra of the VO₂-embedded hybrid MM at different temperatures for a delay time $\Delta\tau$ of 149 ps. At temperatures of 60 °C and 64 °C, it can be seen that only the BDP resonance of the MM appears under a low pump power, as shown in Figs. 5(a) and 5(b). The strength of the resonance decreases with an increase in the optical pump power. However, the resonant frequency barely shifts, which is different from the results for the thermal and electrical stimuli. This is similar to the simulation results shown in Fig. 3, in which we only considered the increase in electrical conductivity

of the VO₂ film. Previous experimental results have shown that the resonance frequency redshifts in the thermal stimulus case, but remains unchanged in a strong THz field [43]. Moreover, the transmission spectrum of the THz-field-induced phase transition is consistent with the electromagnetic simulation results, in which only the change in conductivity of the VO₂ film is considered. The VO₂ phase transition process in the strong THz field is explained by the increase in the carrier concentration, the carrier acceleration of the applied electric field by the Poole-Frenkel effect, and the Joule heat effect resulting from the subsequent electron and lattice coupling. Therefore, we can say that the phase transition of the VO₂ film under the femtosecond pulse stimulus is not a pure thermal effect. Instead, it is caused by the Mott-Peierls phase transition as the concentrations of the light-excited carrier and the light-excited hole in the vicinity of 6 THz exceed their respective threshold values [59]. Even the process and mechanism of phase transition of VO₂ film induced by thermal stimulus, electrical stimulus and optical stimulus are different, the final mode switching results are similar. We compared the simulation and experimental result with different external stimulus in Fig. 6. It can be seen that the simulation with VO₂ conductivity of 4×10^5 S/m and experimental results from thermal effect at 88 °C, electrical stimulus with 0.35 A at room temperature, and optical pump power of 1.68 W at 68 °C are very similar. The two resonant modes appear clearly in the spectrum, which indicates that the MM has changed from BDP mode to SBDP and CTP modes. Therefore, we can say that the electrical conductivities of VO₂ film for these three cases are very similar.

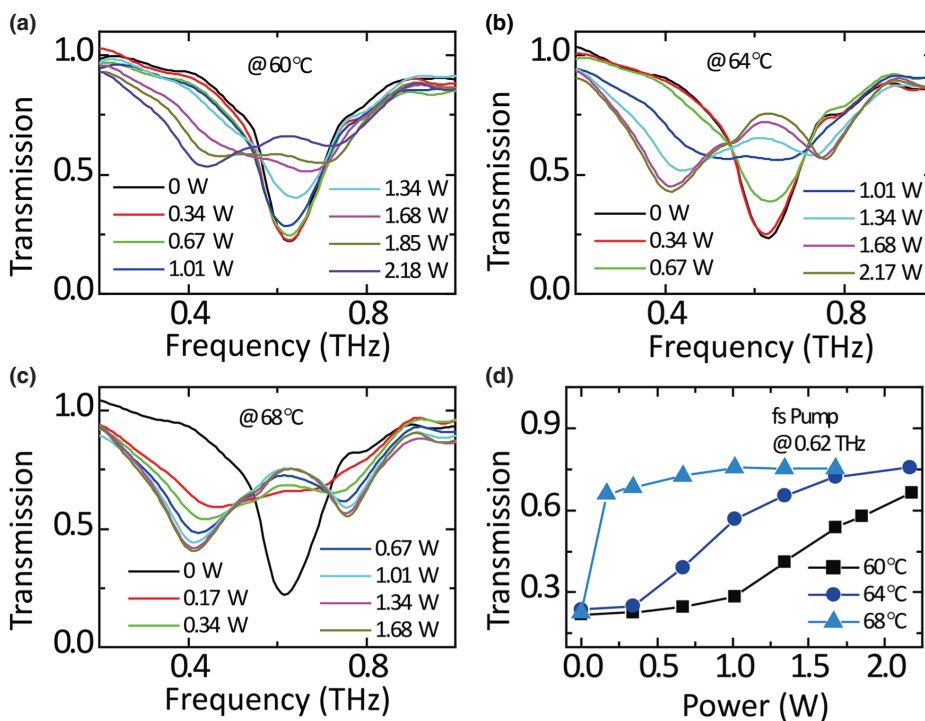


FIG. 5. THz transmission of the VO₂-embedded hybrid MM under an optical stimulus. (a), (b), and (c) represent the THz spectra at 60 °C, 64 °C, and 68 °C, respectively. (d) Transmission vs optical pump power at three temperatures and frequency of 0.62 THz.

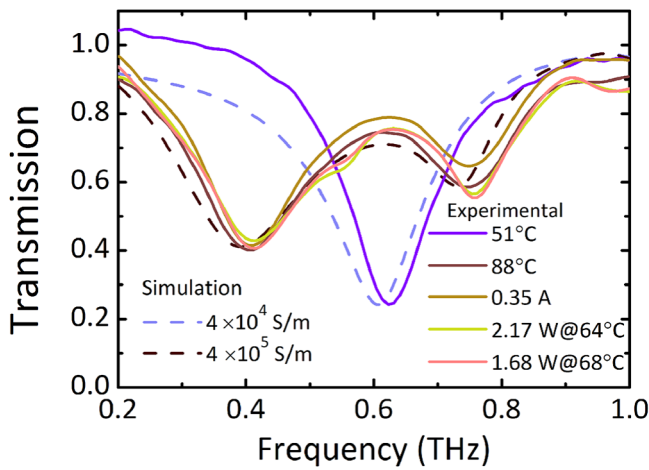


FIG. 6. The THz transmission spectra from simulation (dash line) and experimental results with different external stimulus (solid line), including thermal stimulus at 51 °C and 88 °C, electrical stimulus with 0.35 A at room temperature, and optical stimulus with 2.17 W at 64 °C and 1.68 W at 68 °C.

From Figs. 5(a)–5(c), we can see that the BDP resonance frequency does not shift as the pump power increases below the threshold values. Therefore, it is reasonable to speculate that the dielectric constant of the VO₂ at low pump powers is almost unchanged. Only the conductivity of the film increases. As the pump power increases, the resonant mode eventually changes from BDP mode to CTP and SBDP modes. It can be seen from Fig. 5(c) that the transmission spectrum at 68 °C and 1.68 W in

the optical stimulus case is similar to that in the thermal stimulus case at 88 °C, which means that the electrical conductivities of VO₂ film for these two stimuli are similar. Figure 5(d) shows the THz transmission spectra as a function of the pump power at three temperatures (60 °C, 64 °C, and 68 °C) and a frequency of 0.62 THz. The optical pump power threshold clearly decreases with an increase in temperature. The phase transition threshold power is close to 0 W at the critical temperature of 68 °C.

Using this optical pump–THz probe spectroscopy, we further studied the dynamic response process of the VO₂-embedded hybrid MM. It can be seen from Fig. 7(a) that the THz spectra are basically the same under delay times of –137.7 and 149 ps at 64 °C and a pump power of 1.68 W. In fact, the maximum attainable THz pulse delay is approximately 1 ms. The similar transmission spectra at these delay times indicates that the VO₂ does not revert to the insulating phase in less than 1 ms.

We also measure the THz transmission spectra of our VO₂-embedded MM at 55 °C and a pump power of 2.03 W under several different delay times, as shown in Fig. 7(b), to investigate the dynamics of the THz transmission spectra caused by the phase transition of the VO₂ film. With a negative delay time, the resonance dip exhibits the lowest amplitude and remains almost unchanged as the delay time increases. When the delay time is zero, the pump and probe pulses reach our sample simultaneously. The phase transition of VO₂ is a sub-ps process, thus the amplitude of the resonant dip increases immediately. Note that the shape of the resonance dip is asymmetric. This arises from

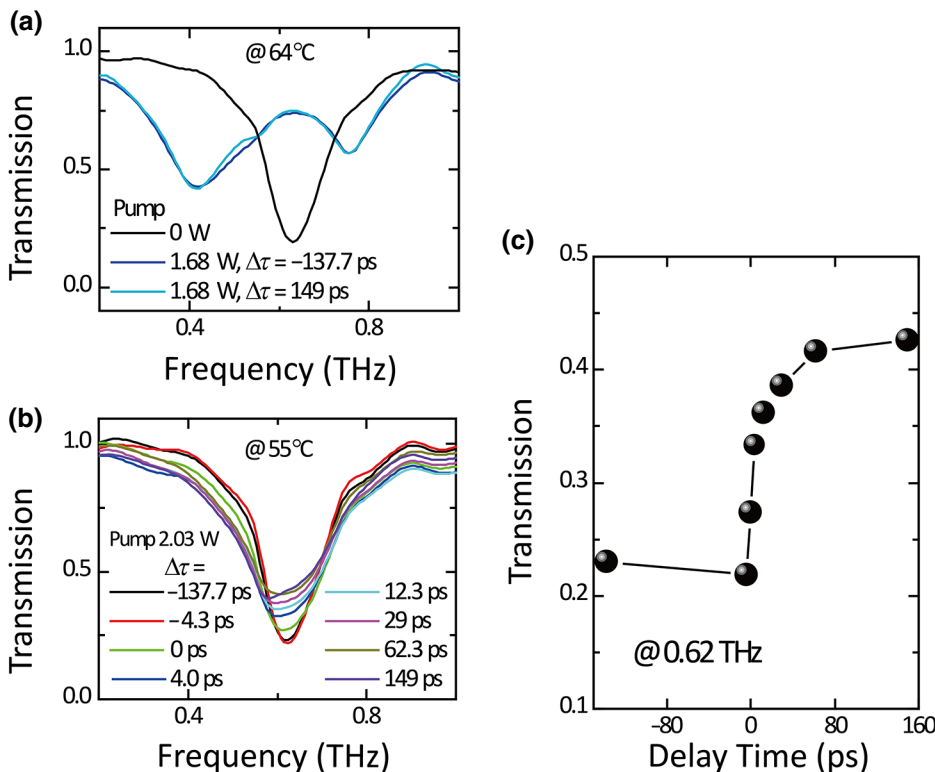


FIG. 7. Optical pump–THz probe measurement results. (a) THz spectra without pump pulse and with a pump pulse of 1.68 W under a delay time of 137.7 and 149 ps, respectively. (b) THz spectra at pump pulse of 2.03 W and different delay times. (c) Transmission vs delay time at 0.62 THz.

the absorption of water vapor in the air (the frequency is 0.56 THz, see [60]). When the delay time is 4 ps, the transmission of the resonant dip increases further. As the delay time increases from 4 to 149 ps, the amplitude of the resonant dip increases slowly. To see this dynamic process clearly, the transmission is plotted with respect to the delay time in Fig. 7(c). This illustrates the whole phase process. The fast VO₂ optical-excited phase transition occurs from 0 to 4 ps. This phase is the contribution of Mott-Peierls phase transition and can produce a metallic phase. The increase in amplitude almost ceases at 62.3 ps. The slow process, lasting about 60 ps, corresponds to the slow phase of the optical excitation of the VO₂ phase transition, which can be explained by the grain growth and connection of the metal phase, that is, a percolation process.

IV. SUMMARY

VO₂ undergoes a metal–insulator transition at around 68 °C, and has a high conductivity in the conducting state and a dynamic conductivity range of five orders of magnitude. In this study, we construct a VO₂-embedded hybrid MM composed of an array of two metal structures connected by VO₂ pads. Using the metal–insulator transition of VO₂, we experimentally demonstrate the mode switching phenomenon in this MM using thermal, electrical, and optical stimuli. The physical reasons for the phase transition are similar for the thermal and electrical stimuli, but different for the optical stimulus. The diversity of the stimuli is favorable in practical applications such as THz modulators, phase-array antennas, and wireless communications, and represent an innovative technique for manipulating THz waves.

ACKNOWLEDGMENTS

This work is supported by the National Key Research and Development Program of China (Grant No. 2017YFA 0700202), Natural Science Foundation of China (Grants No. 61731010, No. 61521001, No. 61671234, No. 61501219, No. 61871212, No. 61701219, and No. 51572042), Science Challenge Project (Grant No. TZ 2018003), Jiangsu Provincial Natural Science Fund (Grant No. BK20170649), and the Fundamental Research Funds for the Central Universities.

C.Z. and G.Z. contributed equally to the work.

-
- [1] Michael Kozziol, It is never too early to thin about 6G, *IEEE Spectrum* (2018).
 - [2] T. Nagatsuma, G. Ducournau, and C. Renaud, Advances in terahertz communication accelerated by photonics, *Nat. Photonics* **10**, 371 (2016).
 - [3] M. Tonouchi, Cutting-edge terahertz technology, *Nat. Photonics* **1**, 97 (2007).

- [4] F. Sizov, THz radiation sensors, *Opto-Electron. Rev.* **18**, 10 (2010).
- [5] H. Tao, W. J. Padilla, X. Zhang, and R. D. Averitt, Recent progress in electromagnetic metamaterial devices for terahertz applications, *IEEE J. Sel. Top. Quantum Electron.* **17**, 92 (2011).
- [6] N. I. Zheludev and Y. S. Kivshar, From metamaterials to metadevices, *Nat. Mater.* **11**, 917 (2012).
- [7] H. T. Chen, W. J. Padilla, J. M. O. Zide, A. C. Gossard, A. J. Taylor, and R. D. Averitt, Active terahertz metamaterial devices, *Nature* **444**, 597 (2016).
- [8] H. T. Chen, J. F. O'Hara, A. K. Azad, A. J. Taylor, R. D. Averitt, D. B. Shrekenhamer, and W. J. Padilla, Experimental demonstration of frequency-agile terahertz metamaterials, *Nat. Photonics* **2**, 295 (2008).
- [9] N. H. Shen, M. Massaouti, M. Gokkavas, J. M. Manceau, E. Ozbay, M. Kafesaki, T. Koschny, S. Tzortzakis, and C. M. Soukoulis, Optically Implemented Broadband Blueshift Switch in the Terahertz Regime, *Phys. Rev. Lett.* **106**, 037403 (2011).
- [10] J. Q. Gu, R. Singh, X. Liu, X. Zhang, Y. Ma, S. Zhang, S. A. Maier, Z. Tian, A. K. Azad, H.-T. Chen, A. J. Taylor, J. Han, and W. Zhang, Active control of electromagnetically induced transparency analogue in terahertz metamaterials, *Nat. Commun.* **3**, 1151 (2012).
- [11] D. Shrekenhamer, W. C. Chen, and W. J. Padilla, Liquid Crystal Metamaterial Absorber, *Phys. Rev. Lett.* **110**, 177403 (2013).
- [12] S. Savo, D. Shrekenhamer, and W. J. Padilla, Liquid crystal metamaterial absorber spatial light modulator for THz applications, *Adv. Opt. Mater.* **2**, 275 (2014).
- [13] W. A. Vitale, M. Tamagnone, N. Émond, B. L. Drogoff, S. Capdevila, A. Skrivervik, M. Chaker, J. R. Mosig, and A. M. Ionescu, Modulated scattering technique in the terahertz domain enabled by current actuated vanadium dioxide switches, *Sci. Rep.* **7**, 41546 (2017).
- [14] D. Wang, L. Zhang, Y. Gu, M. Q. Mehmood, Y. Gong, A. Srivastava, L. Jian, T. Venkatesan, C.-W. Qiu, and M. Hong, Switchable ultrathin quarter-wave plate in terahertz using active phase-change metasurface, *Sci. Rep.* **5**, 15020 (2015).
- [15] M. Reza, M. Hashemi, S. H. Yang, T. Y. Wang, N. Sepulveda, and M. Jarrahi, Electronically-controlled beam steering through vanadium dioxide metasurfaces, *Sci. Rep.* **6**, 35439 (2016).
- [16] C. G. Zhou, P. Dai, J. Wu, B. Jin, Q. Wen, G. Zhu, Z. Shen, C. Zhang, L. Kang, W. Xu, J. Chen, and P. Wu, Broadband and high modulation-depth THz modulator using low bias controlled VO₂-integrated metasurface, *Opt. Express* **25**, 17322 (2017).
- [17] S. Wang, L. Kang, and D. H. Werner, Hybrid resonators and highly tunable terahertz metamaterials enabled by vanadium dioxide (VO₂), *Sci. Rep.* **7**, 4326 (2017).
- [18] D. J. Park, J. H. Shin, K. H. Park, and H. C. Ryu, Electrically controllable THz asymmetric splitloop resonator with an outer square loop based on VO₂, *Opt. Express* **26**, 17397 (2018).
- [19] M. J. Dicken, K. Aydin, I. M. Pryce, L. A. Sweatlock, E. M. Boyd, S. Walavalkar, J. Ma, and H. A. Atwater, Frequency tunable near-infrared metamaterials based on VO₂ phase transition, *Opt. Express* **17**, 18330 (2009).

- [20] M. D. Goldflam, T. Driscoll, D. Barnas, O. Khatib, M. Royal, N. Marie Jokerst, D. R. Smith, Bong-Jun Kim, Giwan Seo, Hyun-Tak Kim, and D. N. Basov, Two-dimensional reconfigurable gradient index memory metasurface, *Appl. Phys. Lett.* **102**, 224103 (2013).
- [21] B. B. Jin, C. H. Zhang, S. Engelbrecht, A. Pimenov, J. B. Wu, Q. Y. Xu, C. H. Cao, J. A. Chen, W. W. Xu, L. Kang, and P. H. Wu, Low loss and magnetic field-tunable superconducting terahertz metamaterial, *Opt. Express* **18**, 17504 (2010).
- [22] H. T. Chen, H. Yang, R. Singh, J. F. O'Hara, A. K. Azad, S. A. Trugman, Q. X. Jia, and A. J. Taylor, Tuning the Resonance in High-Temperature Superconducting Terahertz Metamaterials, *Phys. Rev. Lett.* **105**, 247402 (2010).
- [23] J. Gu, R. Singh, Z. Tian, W. Cao, Q. Xing, J. Han, and W. Zhang, Terahertz superconductor metamaterial, *Appl. Phys. Lett.* **97**, 71102 (2010).
- [24] C. H. Zhang, J. B. Wu, B. B. Jin, Z. M. Ji, L. Kang, W. W. Xu, J. Chen, M. Tonouchi, and P. H. Wu, Low loss terahertz metamaterial from superconducting niobium nitride films, *Opt. Express* **20**, 42 (2012).
- [25] C. Li, C. Zhang, G. Hu, G. Zhou, S. Jiang, C. Jiang, G. Zhu, B. Jin, L. Kang, W. Xu, J. Chen, and P. Wu, Electrically tunable superconducting metamaterial with low insertion loss and high switchable ratios, *Appl. Phys. Lett.* **109**, 022601 (2016).
- [26] C. Li, J. B. Wu, S. L. Jiang, R. F. Su, C. H. Zhang, C. T. Jiang, G. C. Zhou, B. B. Jin, L. Kang, W. W. Xu, J. Chen, and P. H. Wu, Electrical dynamic modulation of THz radiation based on superconducting metamaterials, *Appl. Phys. Lett.* **111**, 092601 (2017).
- [27] E. Carrasco, M. Tamagnone, and J. Perruisseau-Carrier, Tunable graphene reflective cells for THz reflectarrays and generalized law of reflection, *Appl. Phys. Lett.* **102**, 104103 (2013).
- [28] B. Sensale-Rodriguez, R. Yan, M. M. Kelly, T. Fang, K. Tahy, W. S. Hwang, D. Jena, L. Liu, and H. G. Xing, Broadband graphene terahertz modulators enable by intraband transitions, *Nat. Commun.* **3**, 780 (2012).
- [29] W. Yang, C. La-O-Vorakiat, X. Qiu, J. Liu, P. Deorani, K. Banerjee, J. Son, Y. Chen, E. E. Chia, and H. Yang, Graphene terahertz modulators by ionic liquid gating, *Adv. Mater.* **27**, 1874 (2015).
- [30] Z. Yang, C. Ko, and S. Ramanathan, Oxide electronic utilizing ultrafast metal-insulator transitions, *Annu. Rev. Mater. Res.* **41**, 337 (2011).
- [31] P. Mandal, A. Speck, C. Ko, and S. Ramanathan, Terahertz spectroscopy studies on epitaxial vanadium dioxide thin films across the metal-insulator transition, *Opt. Lett.* **36**, 1927 (2011).
- [32] P. Uhd. Jepsen, B. M. Fischer, A. Thoman, H. Helm, J. Y. Suh, R. Lopez, and R. F. Haglund Jr, Metal-insulator phase transition in a VO₂ thin film observed with terahertz spectroscopy, *Phys. Rev. B* **74**, 205103 (2006).
- [33] J. Kyoung, M. Seo, H. Park, S. Koo, H. S. Kim, Y. Park, B. J. Kim, K. Ahn, N. Park, and H. T. Kim, Giant nonlinear response of terahertz nanoresonators on VO₂ thin film, *Opt. Express* **18**, 16452 (2010).
- [34] A. Pashkin, C. Kübler, H. Ehrke, R. Lopez, A. Halabica, R. F. Haglund Jr, R. Huber, and A. Leitenstorfer, Ultrafast insulator-metal phase transition in VO₂ studied by multiterahertz spectroscopy, *Phys. Rev. B* **83**, 195120 (2011).
- [35] H. Zhang, C. Li, C. Zhang, X. Zhang, J. Gu, B. Jin, J. Han, and W. Zhang, Experimental study on the transition of plasmonic resonance modes in double-ring dimers by conductive junctions in the terahertz regime, *Opt. Express* **24**, 27415 (2016).
- [36] O. Pérez-González, N. Zabala, A. G. Borisov, N. J. Halas, P. Nordlander, and J. Aizpurua, Optical spectroscopy of conductive junctions in plasmonic cavities, *Nano Lett.* **10**, 3090 (2010).
- [37] J. Fontana and B. R. Ratna, Highly tunable gold nanorod dimer resonances mediated through conductive junctions, *Appl. Phys. Lett.* **105**, 11107 (2014).
- [38] Lei Wang, X. W. Lin, W. Hu, G. H. Shao, P. Chen, and Y. Q. Lu, Broadband tunable liquid crystal terahertz waveplates driven with porous graphene electrodes, *Light Sci. Appl.* **4**, e253 (2015).
- [39] N. K. Emami, T.-F. Chung, X. Ni, A. V. Kildishev, Y. P. Chen, and A. Boltasseva, Electrically tunable damping of plasmonic resonances with graphene, *Nano Lett.* **12**, 5202 (2012).
- [40] T. Driscoll, S. Palit, M. M. Qazilbash, and M. Brehm, Dynamic tuning of an infrared hybrid-metamaterial resonance using vanadium dioxide, *Appl. Phys. Lett.* **93**, 24101 (2008).
- [41] Y. Xiong, Q. Y. Wen, Z. Chen, W. Tian, T. L. Wen, Y. L. Jing, Q. H. Yang, and H. W. Zhang, Tuning the phase transitions of VO₂ thin films on silicon substrates using ultrathin Al₂O₃ as buffer layers, *J. Phys. D: Appl. Phys.* **47**, 455304 (2014).
- [42] See Supplemental Material at <http://link.aps.org/supplemental/10.1103/PhysRevApplied.11.054016> for the details of experimental setup and methods.
- [43] M. Liu, H. Y. Hwang, H. Tao, A. C. Strikwerda, K. Fan, G. R. Keiser, A. J. Sternbach, K. G. West, S. Kittiwatanakul, J. Lu, S. A. Wolf, F. G. Omenetto, X. Zhang, K. A. Nelson, and R. D. Averitt, Terahertz-field-induced insulator-to-metal transition in vanadium dioxide metamaterial, *Nature* **487**, 345 (2012).
- [44] J. Leroy, A. Crunteanu, A. Bessaudou, F. Cosset, C. Champeaux, and J.-C. Orlianges, High-speed metal-insulator transition in vanadium dioxide films induced by an electrical pulsed voltage over nano-gap electrodes, *Appl. Phys. Lett.* **100**, 213507 (2012).
- [45] K. Hyun-Tak, B. G. Chae, D. H. Youn, S. L. Maeng, G. Kim, K. Y. Kang, and Y. S. Lim, Mechanism and observation of Mott transition in VO₂-based two- and three-terminal devices, *New J. Phys.* **6**, 52 (2004).
- [46] S. Hormoz and S. Ramanathan, Limits on vanadium oxide Mott metal-insulator transition field-effect transistors, *Solid State Electron.* **54**, 654 (2010).
- [47] D. H. Qiu, Q. Y. Wen, Q. H. Yang, Z. Chen, Y. L. Jing, and H. W. Zhang, Electrically-driven metal-insulator transition of vanadium dioxide thin films in a metal-oxide-insulator-metal device structure, *Mater. Sci. Semicond. Process.* **27**, 140 (2014).

- [48] G. Stefanovich, A. Pergament, and D. Stefanovich, Electrical switching and Mott transition in VO₂, *J. Phys.: Condens. Matter* **12**, 8837 (2000).
- [49] A. L. Pergament, P. P. Boriskov, A. A. Velichko, and N. A. Kuldin, Switching effect and the metal–insulator transition in electric field, *J. Phys. Chem. Solids* **71**, 874 (2010).
- [50] B. Mayer, C. Schmidt, A. Grupp, J. Buehler, J. Oelmann, R. E. Marvel, R. F. Haglund Jr, T. Oka, D. Brida, A. Leitenstorfer, and A. Pashkin, Tunneling breakdown of a strongly correlated insulating state in VO₂ induced by intense multiterahertz excitation, *Phys. Rev. B* **91**, 235113 (2015).
- [51] P. Markov, R. E. Marvel, H. J. Conley, K. J. Miller, R. F. Haglund Jr, and S. M. Weiss, Optically monitored electrical switching in VO₂, *ACS Photonics* **2**, 1175 (2015).
- [52] S. Kumar, M. D. Pickett, J. P. Strachan, G. Gibson, Y. Nishi, and R. S. Williams, Local temperature redistribution and structural transition during Joule-heating-driven conductance switching in VO₂, *Adv. Mater.* **25**, 6128 (2013).
- [53] A. Joushaghani, J. Jeong, S. Paradis, D. Alain, J. S. Aitchison, and J. K. S. Poon, Electronic and thermal effects in the insulator-metal phase transition in VO₂ nano-gap junctions, *Appl. Phys. Lett.* **105**, 231904 (2014).
- [54] J. Yoon, H. Kim, B. S. Mun, C. Park, and H. Ju, Investigation on onset voltage and conduction channel temperature in voltage-induced metal-insulator transition of vanadium dioxide, *J. Appl. Phys.* **119**, 124503 (2016).
- [55] B. S. Mun, J. Yoon, S.-K. Mo, K. Chen, N. Tamura, C. Dejoie, M. Kunz, Z. Liu, C. Park, K. Moon, and H. Ju, Role of joule heating effect and bulk-surface phases in voltage-driven metal-insulator transition in VO₂ crystal, *Appl. Phys. Lett.* **103**, 61902 (2013).
- [56] J. Hebling, K. L. Yeh, M. C. Hoffmann, B. Bartal, and K. A. Nelson, Generation of high-power terahertz pulses by tilted-pulse-front excitation and their application possibilities, *J. Opt. Soc. Am. B* **25**, B6 (2008).
- [57] H. Hirori, A. Doi, F. Blanchard, and K. Tanaka, Single-cycle terahertz pulses with amplitudes exceeding 1 MV/cm generated by optical rectification in LiNbO₃, *Appl. Phys. Lett.* **98**, 091106 (2011).
- [58] D. J. Hilton, R. P. Prasankumar, S. Fourmaux, A. Cavalleri, D. Brassard, M. A. El Khakani, J. C. Kieffer, A. J. Taylor, and R. D. Averitt, Enhanced Photosusceptibility Near T_c for the Light-Induced Insulator-to-Metal Phase Transition in Vanadium Dioxide, *Phys. Rev. Lett.* **99**, 226401 (2007).
- [59] T. L. Cocker, L. V. Titova, S. Fourmaux, G. Holloway, H. C. Bandulet, D. Brassard, J. C. Kieffer, M. A. El Khakani, and F. A. Hegmann, Phase diagram of the ultrafast photoinduced insulator-metal transition in vanadium dioxide, *Phys. Rev. B* **85**, 155120 (2012).
- [60] M. van Exter, C. Fattinger, and D. Grischkowsky, Terahertz time-domain spectroscopy of water vapor, *Opt. Lett.* **14**, 1128 (1989).